Slower long-term coastal warming drives dampened trends in coastal marine heatwave exposure

Maxime Marin[1,2,3], Nathaniel L. Bindoff[1,2,4,5], Ming Feng[3], Helen E. Phillips[1,2,4]

[1] Institute for Marine and Antarctic Studies, University of Tasmania, Hobart, TAS 7001, Australia

[2] ARC Centre of Excellence for Climate Extremes, Hobart TAS 7001

[3] CSIRO Oceans and Atmosphere, Indian Ocean Marine Research Centre, Crawley, WA 6009, Australia

[4] Australian Antarctic Program Partnership, Hobart, TAS 7001, Australia

[5] CSIRO Oceans and Atmosphere, Hobart, TAS 7001, Australia

Key Points

- **First global assessment of coastal and offshore differences of MHW metrics using an ensemble approach**
- **Slower onshore SST warming trends drive depressed MHW trends relative to offshore**
- **Results were consistent across observations and not restricted to upwelling regions.**
- **Models did not agree well with observation, despite providing necessary tools to[1] understand driving processes.**

Keywords: Marine HeatWaves (MHW), coastal cooling, cross-shore gradients, ensemble approach, upwelling change

Abstract

Long-term temperature changes drive coastal Marine Heat Waves (MHW) trends globally. Here, we provide a more comprehensive global analysis of cross-shore gradients of MHW and SST changes using an ensemble of three satellite SST products during recent decades. Our analysis reveals depressed onshore SST trends in more than 2/3 of coastal pixels, including both eastern and western boundary current systems. These were well correlated with depressed trends of MHW exposure and severity, ranging from a -2 to -10 decrease in MHW days per decade and a –2.5 to –15°C.days per decade decrease in cumulative intensity. Results were consistent across all satellite products, indicating that these cross-shore gradients are a robust feature of observations. ERA reanalysis data shows that neither air-sea heat fluxes nor wind driven upwelling were found to be consistent drivers. Global ocean circulation models (OFAM3 and ACCESS-OM2) have limited ability to simulate the depressed

[1]

onshore trends. A heat budget analysis performed in the Chilean coast region, where models agree with observations, showed that the gradient of temperature change was controlled by an onshore increase of longwave radiative cooling, despite an increase in upwelling. This highlights the complexity of small-scale coastal ocean-atmosphere feedbacks, which coarser resolution climate models do not resolve. Here, we show that global coastal regions may act as thermal refugia for marine ecosystems from aspects of climate change and pulsative (MHW) changes. Contrary to the literature, our results suggest that driving mechanisms are region dependant, stressing the necessity to improve climate models resolution.

Plain Language Summary

We analyse differences of the long-term change of MHW and Sea Surface Temperatures (SST) between coastal and offshore regions, using three different satellite SST products. We found that, in 2/3 of cases, the rate of change of SST in coastal regions was lower than offshore. As most regions have experienced recent warming, this means that the warming was slower near the coast. This phenomenon, was observed along most coastlines. Slower rates of SST change were well correlated with slower rates of MHW change. Our results were observed in all three SST products, indicating that this phenomenon is not due to errors associated with satellite measurements. Using reconstructed atmospheric data, we show that neither air-sea exchanges nor wind driven upwelling could explain the smaller coastal change consistently. Global ocean circulation models (OFAM3 and ACCESS-OM2) were not able to simulate this signal in every region. However, results from a heat budget analysis performed in regions of agreement highlighted the complexity of ocean-atmosphere exchanges happening on a small scale, that coarse resolution climate models do not resolve. Here, we demonstrate that global coastal regions may act as a refugia for marine ecosystems under increasing threat from rising temperatures.

Introduction

A Marine HeatWave (MHW) is an extreme oceanic heat event that has potentially devastating consequences on marine ecosystems and negative impacts on the fisheries industry economy. Such events have been found to be increasing in occurrence, intensity and duration globally (Frölicher et al., 2018; Marin et al., 2021; E. C. J. Oliver et al., 2018). These changes have been largely attributed to a rise in mean ocean temperature (Laufkötter et al., 2020; Marin et al., 2021; E. C. J. Oliver, 2019). In the context of climate change, most scenarios project MHW metrics to further increase (Bindoff et al., 2019; Frölicher et al., 2018; Hayashida et al., 2020; E. Oliver et al., 2019), possibly reaching a state of "permanent" MHW by the end of the century, assuming a constant threshold (Oliver et al., 2019).

Despite recent efforts to understand MHW variability in the global ocean, there

is limited knowledge of the behaviour of MHWs in coastal regions. Coastal oceanographic processes and variability differ greatly from offshore waters, inducing differences in MHW characteristics. Increasing our understanding of coastal MHWs is critical for proper sustainability of marine ecosystems, as coastal ecosystems are the richest and most complex in the ocean (Costello & Chaudhary, 2017). Recent changes in temperatures have been the most severe source of impact on coastal ecosystems (Halpern et al., 2008), and the projected rise of ocean temperatures (Bindoff et al., 2019) will further increase their vulnerability. To date, only two studies provided an assessment of MHWs in coastal areas. Hu (2021) investigated the relationship of coastal MHWs with urban thermal changes. The author found a considerable strengthening of coastal MHWs during the last 4 decades in most of their 38 locations studied. MHW trends were consistent with increased air temperatures, increased moisture and decreased winds, suggesting a strong coupling of coastal ocean and land during extreme heat events. Marin et al. (2021) provided a global assessment of coastal MHWs by selecting all coastal pixels in multiple global satellite Sea Surface Temperature (SST) datasets. Their study showed that similarly to the global ocean, coastal MHW metrics had been largely increasing during the past decades, except for MHW intensity. In addition, linear trends were mostly explained by the long-term change in the mean SST, confirming that coastal ecosystems are expected to be under increasing pressure from MHW events in the context of climate change. Although the mean state and long-term trends of MHWs were found to be similar amongst all SST products, the authors found regional differences linked to differences in internal variability which drive observed decadal trends.

As long-term SST trends are the main driver of MHW trends, the SST trend difference between coastal and offshore (referred to onshore-offshore hereafter) waters can provide insights into the cross-shore gradient of MHW long-term trends. Multiple studies investigated coastal long-term SST changes and found that the global ocean warming trend was dampened along coastlines (Santos, deCastro, et al., 2012; Santos et al., 2016; Santos, Gomez-Gesteira, et al., 2012; Seabra et al., 2019; Varela et al., 2016, 2018). This cooling tendency was most evident in Eastern Boundary Current (EBC) regions, associated with coastal upwelling. Varela et al. (2018) reported that 92% of coastal locations within upwelling systems were associated with nearshore decreased warming or increased cooling compared to offshore equivalents. Differences amongst EBCs were investigated by Seabra et al. (2019) who found that Pacific EBC SSTs had an overall cooling trend, increased near-shore, while Atlantic EBC SSTs had an overall warming trend, dampened near-shore.

The decreased/increased coastal warming/cooling is believed to be a consequence of an increase in upwelling as predicted by the theory of (Bakun, 1990). Bakun hypothesised that global warming would increase coastal thermal gradients due to a slower warming rate of the ocean. The increased SST and land temperature gradients across the ocean-land boundary have been attributed to climate change and increased greenhouse gases in the atmosphere (Bindoff et

al., 2014; Lambert et al., 2011; Sutton et al., 2007; Wallace & Joshi, 2018). Increased thermal gradients across the ocean-land boundary would in turn force an increase in upwelling favourable winds, therefore increasing upwelling mass transport along most EBC systems. Following Bakun's theory, there were numerous attempts to quantify changes in upwelling during the last decades, using both models and observations (Abrahams et al., 2021; Bonino, di Lorenzo, et al., 2019; García-Reyes & Largier, 2010; Narayan et al., 2010; Patti et al., 2010; Rykaczewski & Checkley, 2008; Seo et al., 2012; Sydeman et al., 2014; Varela et al., 2015). These studies produced conflicting results (Varela et al., 2015) demonstrating a lack of consensus on recent trends of EBC upwellings. Discrepancies in results are attributed to multiple factors, including differences of datasets (i.e., resolution and time coverage), differences in methodologies used to derive upwelling measures (Abraham et al., 2021) and biases of ocean models, which can struggle to correctly simulate coastal upwellings due to their coarse resolution (Bonino, Masina, et al., 2019; Small et al., 2015). Perhaps more importantly, the relationship between an increase of upwelling mass transport with a decrease in SST warming remains uncertain. Surface stratification is expected to increase in a warming climate, reducing surface mixing and decreasing the surface signature (Brady et al., 2019; García-Reyes & Largier, 2010).

Aligned with evident across-shore differences of long-term SST trends, Varela et al., (2021) explored its relationship with differences of MHW occurrence trends in EBUs. The authors showed that the 1982-2018 change of MHW occurrence in offshore areas, unaffected by upwelling, was consistently higher to that of coastal pixels in all EBCs. The value of the offshore long-term MHW occurrence trend was found to be 8.01 5.65 6.940, 0.35 and 8.9 MHW days year^{-1} decade^{-1} larger than coastal pixels for the Benguela, Canary, Chile, Peru and California systems, respectively. As is the case with most MHW studies, Varela et al. derived their results from the NOAA OISST v2.1 product (Huang et al., 2021). In fact, most studies highlighting dampened onshore SST trends were also exclusively using the NOAA product. It is well known that SST global gap-free daily satellite products have inherent biases linked to the specificity of their algorithms and the nature of observations they assimilate (Fiedler et al., 2019). Comparing results from the NOAA OISST product with other similar products is necessary to ensure that results are not attributable to biases in the NOAA OISST product (Figure 1).

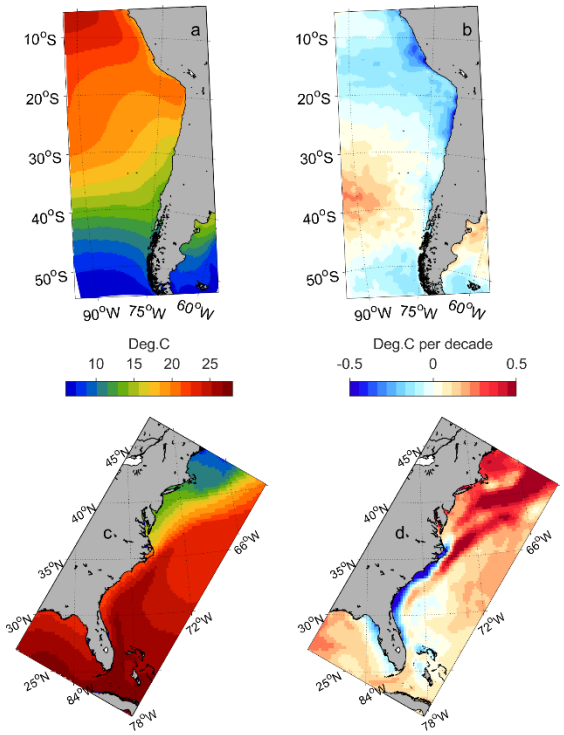

Figure 1: Example of onshore-offshore differences. Mean SST (a, c) and associated long-term SST linear trends (b, d) in the south-eastern Pacific (a-b) and north-western Atlantic (c-d). SST means and trends were derived from the NOAA OISST v2.1 product during the 1982-2014 period.

In that context, our study aims at exploring the relationship between SST and MHW changes during the past decades, by comparing coastal with offshore locations globally. The analysis is carried out using multiple global SST satellite products, in part to assess the impact of satellite product biases, but also to ensure that the overall ensemble results in our best estimate of the underlying change with biases taken into account. This approach is identical to that used in IPCC for the assessment of climate change trends and in the use of CMIP simulations (Bindoff et al., 2014). MHW trends are considered for a variety of metrics as their long-term changes are not uniform (Marin et al., 2021). In addition, we use outputs from two global ocean circulation models to evaluate these models' ability to capture cross-shore gradients of SST and MHW changes. Finally, we use a combination of atmospheric re-analysis outputs and a depth-integrated heat budget analysis of long-term temperature changes to provide insights into the processes responsible for long-term cross-shore trend differences.

Methods

Data

SST satellite datasets

SST Observation datasets used in this study are 3 daily global satellite SST products (L4 gap-free, gridded) including the National Oceanic and Atmospheric Administration (NOAA) Advanced very High Resolution Radiometer (AVHRR) ¼ degree daily Optimum Interpolation SST (OISST) v2.1 Analysis data, available from September 1, 1981 to present. This new version was released in April 2020 featuring major improvements in the data assimilation process and satellite input following a degrading data quality of v2.0 from January 1, 2016 (Huang et al., 2021). OISST has a spatial resolution of 0.25°, a depth of ~0.2m and includes both day and night measurements, ignoring the diurnal cycle (Reynolds et al., 2007). NOAA OISST is the most widely used SST product in climate research, especially in MHW research (Marin et al., 2021).

The second satellite SST product used is the Japan Meteorological Agency (JMA) Merged satellite and in-situ data Global Daily (MGD) SST (Sakurai et al., 2005), available from Jan 1981 to present. MGD uses both AVHRR and Advanced Microwave Scanning Radiometer (AMSR) measurements, with a spatial resolution of 0.25°. Both daytime and night-time measurements are averaged after removing the day-night difference, removing the diurnal cycle, which gives MGD a depth of ~10m (foundation temperature).

The European Space Agency (ESA) SST Climate Change Initiative (CCI) Analysis Climate Data Record v2.1 (Merchant et al., 2019) is the third observational satellite SST product used in the study. Data are available from Jan 1981 to Dec 2016, with a spatial resolution of 0.05°. CCI only incorporates radiometer measurements from AVHRR and Advanced Along-Track Radiometer (AATSR) sensors. SST measurements are converted from Skin temperature to a nominal 0.2m temperature estimation. The diurnal cycle is removed by adjusting temperature measurements to the nearest of 10:30 or 22:30 local mean solar time, which is a good approximation of the mean daily temperature (Merchant et al., 2019).

There is nowadays a variety of daily global satellite SST products, with varying degrees of agreement with in-situ observations (Beggs, 2019). Comparisons with Argo floats revealed that neither OISST, MGD or CCI performed the best in terms of mean or standard deviation bias (Fiedler et al., 2019; Woo & Park, 2020). However, those 3 SST products were chosen due to their longer time coverage, spanning at least 35 years, which is adequate for decadal trend studies. All include temperature adjustments to a range of in-situ data including ship measurements, buoys readings and moorings. Coastal long-term trends of most MHW metrics were found to be globally consistent across those products (Marin et al., 2021). Nevertheless, there are well described differences between all SST products, stressing the importance of investigating an ensemble of products to

better assess associated uncertainties.

Atmospheric observations

Outputs from two European Centre for Medium Range Weather Forecast (ECMWF) climate reanalysis products were analysed to investigate the driving mechanisms of long-term SST changes. Monthly averages of surface radiative (shortwave and longwave) and turbulent (sensible and latent) heat fluxes from ERA5 (Hersbach et al., 2020) were retrieved at a horizontal resolution of 0.25°. In addition, 10-m zonal and meridional wind components as well as total cloud cover from ERA-Interim (Dee et al., 2011) were also used at a resolution of 0.75°. ERA5 uses an improved version of ECMWF data assimilation system and ingests a larger volume of better quality observations, to produce outputs at a higher resolution than its ERA-Interim predecessor. Such updates are expected to significantly improve surface energy partitioning.

Ocean General Circulation Models

Monthly outputs from two ocean general circulation models were compared with observations and used to investigate the drivers of long-term trend differences.

OFAM3 The Ocean Forecasting Australia Model version 3 (OFAM3; Oke et al., 2013) is a near global configuration of the Geophysical Fluid Dynamic Laboratory (GFDL) Modular Ocean Model version 4p1d (Griffies et al., 2004). The model has a spatial resolution of 1/10° spanning all longitudes and latitudes between 75°S and 75°N. OFAM3 vertical coordinate is z-star, with 51 vertical levels at a 5m resolution from the surface to 10m resolution at 200m depth. The vertical resolution in deeper layers increases greatly as the focus of OFAM3 was primarily the upper ocean conditions. The minimum number of vertical levels in the model was set to three, resulting in a minimum depth of 15m.

The model is forced with 1.5° resolution, 3-hourly surface fluxes, freshwater and momentum fluxes derived from the European Centre for Medium-Range Weather Forecasts Reanalysis (ERA)-interim product (Dee et al., 2011). Turbulent air-sea fluxes (i.e., sensible and latent heat flux) are calculated with bulk formulae according to (Large & Yeager, 2004). Penetrating short-wave radiations is calculated according to a single exponential decay law, using penetration depth based on SeaWIFS Kd-490 (Z.-P. Lee et al., 2005). Surface salinity is relaxed to monthly averaged salinity fields from the CSIRO Atlas of Regional Seas (CARS; Ridgway et al., 2002) climatology, with a restoring time of 180 days. The simulation was initialised from the CARS temperature and salinity climatology and was spun up using the 1979 forcing for 3 years. Model outputs are available from January 1979 to December 2014.

Mixing parametrisations of vertical viscosity and diffusivity in OFAM3 use the KPP mixed layer scheme by Large et al. (1994). Tidal mixing parametrisation is added according to Lee et al. (2006), varying with the amplitude of the

dominant local tidal components. Horizontal viscosity is resolution and state dependant, using a biharmonic Smagorinsky scheme (Griffies & Hallberg, 2000) The model does not include explicit horizontal diffusion.

ACCESS-OM2 The Australian Community Climate and Earth System Simulator (ACCESS) ocean-sea ice model version 2 (Kiss et al., 2020) is the new version of the ocean-ice component of the fully coupled (atmosphere-land-ocean-sea ice) ACCESS-CM2 model. The ocean model component is a configuration of the GFDL MOM version 5.1 (https://mom-ocean.github.io). ACCESS-OM2 has been configured at three different horizontal resolutions: 1° resolution (ACCESS-OM2), 0.25° resolution (ACCESS-OM2-025), and a 0.1° resolution (ACCESS-OM2-01, referred to ACCESS-OM2 therein), used in this study. ACCESS-OM2 uses an orthogonal curvilinear Arakawa B horizontal grid, with velocity components located at the northeast corner of tracer cells. The model uses a z-star vertical coordinate, with 75 vertical levels and 1.1m resolution at the surface, increasing to ~200m at the bottom. horizontal resolutions: 1° resolution (ACCESS-OM2), 0.25° resolution (ACCESS-OM2-025), and a 0.1° resolution (ACCESS-OM2-01, referred to ACCESS-OM2 therein), used in this study. ACCESS-OM2 uses an orthogonal curvilinear Arakawa B horizontal grid, with velocity components located at the northeast corner of tracer cells. The model uses a z-star vertical coordinate, with 75 vertical levels and 1.1m resolution at the surface, increasing to ~200m at the bottom.

ACCESS-OM2 is forced with prescribed atmospheric conditions derived from the 55-year Japanese Reanalysis for driving ocean v1.3 (JRA-do) at a 55 km and 3-hourly resolution (Tsujino et al., 2018), covering 1958 to 2018. Prescribed variables include precipitation, downward surface longwave and shortwave fluxes, sea level pressure, 10m wind velocity components, 10m specific humidity and the 10m air temperature. Freshwater fluxes are also provided by JRA-do at a resolution of 0.25°. Surface fluxes are computed by the Los Alamos Sea Ice model version 5.1 (CICE5) component of ACCESS-OM2. Penetrating shortwave radiation is calculated based on Manizza et al. (2005), which also uses SeaWIFS Kd-490 to estimate its penetration coefficients. ACCESS-OM2 uses the same bulk formulae as OFAM3 to calculate turbulent heat fluxes (Large & Yeager, 2004). Surface wind stress is adjusted relative to the ocean surface velocity. SSS is restored using the interpolated 0.25° World Ocean Atlas 2013 (WOA13) v2 monthly climatology, with a time scale set by the piston velocity of 33 meters per 300 days. Both vertical and horizontal mixing parametrisations in ACCESS-OM2 are the same as in OFAM3, with the addition of bottom-enhanced internal tidal mixing parametrisation following Simmons et al. (2004). ACCESS-OM2 uses a 40-year spin-up of the 1984/1985 year, which was chosen due to its neutral modes of variability (Stewart et al., 2020).

Onshore/offshore differentiation

Coastal (termed onshore hereafter) pixels were derived as the closest non-land pixel based on the land identification mask of each dataset. Corresponding offshore pixels were chosen as pixels whose centroids were closest to a point situated 150 km away from the onshore pixel, perpendicular to the coast. The orientation of the coastline at each coastal point was calculated using the relative orientation of the two most adjacent onshore points from each dataset, resulting in slightly different coastline orientations and onshore and offshore coordinates for each dataset.

Offshore pixels situated at a closer distance to another coastal pixel were not selected, removing the coastal pixel from the analysis. Once an offshore pixel was successfully selected, the area average of pixels whose centroids were located within a 20km radius from the original offshore pixel was computed for each day, to remove any sub-mesoscale variability.

The analysis was performed for each onshore and offshore pixel separately. The lowest resolution products (OISST and MGD) yielded more than 13000 onshore points, while the highest resolution product (CCI) had more than 60000 onshore points. Results were spatially averaged for the main upwelling regions, as defined by Varela et al. (2018), as well as Western Boundary Current (WBC) regions for comparison (Figure 2). The list of all boundary regions and their coordinates are summarised in Table 1.

Table 1: Coordinates of boxes defining the regions used in this study. Box coordinates for upwelling systems were defined based on Varela et al. (2018).

Upwelling Systems	**Coordinates**
Canary (CAN)	{(12.5°W-34°N) ; (5°W–31°N) ; (15°W-21°N) ; (22°W–21°N)}
California (CAL)	{(42°W-20°S) ; (35°W–20°S) ; (48°W-32°S) ; (53°W–32°S)}
Chile (CHIL)	{(80°W-13°S) ; (68°W–13°S) ; (70°W-40°S) ; (80°W–40°S)}
South Benguela (SBEN)	{(10°E-24°S) ; (16°E–24°S) ; (22°E-33°S) ; (15°E–33°S)}
North Benguela (NBEN)	{(8°E-17°S) ; (14°E–17°S) ; (16°E-21°S) ; (9°E–21°S)}
Java-Sumatra (JS)	{(100°E-4°S) ; (104°E–4°S) ; (106.5°E-6.5°S) ; (114°E–10°S) ; (106°E–8°S)}
Somalia (SOM)	{(49°E-11°N) ; (54°E–12°N) ; (50°E-3°N) ; (45°E–3°S)}
Western Boundary Systems	
Kuroshio (KUR)	{(139°E-36°N) ; (142°E–35°N) ; (129°E-29.5°N) ; (131°E–32.5°S)}
East Australian Current (EAC)	{(149°E-32°S) ; (155°E–32°S) ; (150°E-44°S) ; (147°E–42°S)}
Gulf Stream (GS)	{(80°W-37°N) ; (73°W–35°N) ; (80°W-27°N) ; (83°W–31°S)}
Brazil (BRA)	{(42°W-20°S) ; (35°W–20°S) ; (48°W-32°S) ; (53°W–32°S)}

MHW identification

MHW events at both onshore and offshore pixels were identified according to the widely accepted Hobday et al. (2016) definition, using its MATLAB im-

plementation (Zhao & Marin, 2019). A MHW event is therefore flagged if the temperature reaches the 90$^{\text{th}}$ percentile based on an 11-day window climatology for a minimum of 5 days. Here, the baseline climatology was set as 1982-2014, covering 33 years. This definition allows the derivation of several metrics such as the duration and intensity of each event, the frequency of events per year, MHW exposure expressed in MHW days per year, cumulative intensity (°C.days) and Yearly Cumulative Intensity (YCI), being the sum of cumulative intensity of all events within a year (°C.days). In this study, we focus on the MHW exposure and YCI metrics. Those metrics combine the effects of event frequency, duration and intensity (for YCI), which provides a more complete measure of heat stress for marine systems. For completeness, results from all other MHW metrics are included in the supplementary information.

Heat Budget

A heat budget analysis was performed using OFAM3 model outputs to compare the relative contribution of air-sea heat flux, oceanic advection and other oceanic processes in driving long-term changes of near-surface water temperature. Following Oliver et al. (2017), the volume average temperature tendency equation over a volume V defined by a depth h and a rectangular area A can be expressed as:

$$\frac{\partial \langle T \rangle}{\partial t} = \underbrace{\langle -\mathbf{u}.\nabla_h T \rangle}_{\text{AdvH}} - \underbrace{\langle w \frac{\partial T}{\partial z} \rangle}_{\text{AdvV}} + \underbrace{\frac{1}{A}\int^A \frac{Q}{h}\ \mathrm{dA}}_{Q_T} + \underbrace{\langle \nabla_h.(\kappa_h \nabla_h T) - \kappa_v \frac{\partial T}{\partial z} \rangle}_{\text{Res}} + \varepsilon \qquad [1]$$

Where $\langle - \rangle = \frac{1}{V}\int^V \mathrm{dV}$, T is the temperature, $\mathbf{u}$ is the horizontal velocity vector, $\nabla_h$is the horizontal gradient operator, w is the vertical velocity, Q is the net air-sea heat flux, κ_h and κ_v are the horizontal and vertical diffusivity coefficients, and ε is the residual.

The net downward air-sea heat flux at the surface of the ocean (Q_{surf}) can be decomposed as:

$$Q_{\text{surf}} = Q_{\text{sw}} + Q_{\text{lw}} + Q_{\text{ss}} + Q_{\text{lat}} \qquad [2]$$

Where Q_{sw} is the net downward surface shortwave radiation, Q_{lw} is the net downward surface longwave radiation, Q_{sh} is the sensible heat flux and Q_{lat} is the latent heat flux. All but Q_{sw} are typically assimilated by the ocean model in the skin layer (~mm thickness) and then redistributed within the mixed layer through vertical mixing. Shortwave radiations however penetrate the water column and warm water parcels accordingly. Therefore, Q is expressed as:

$$Q = Q_{\text{surf}} - [Q_{\text{sw}}]_{-h} \qquad [3]$$

In this study, we aim to quantify the relative contribution of advection, air-sea heat flux and all other remaining ocean processes from the model (e.g., mixing and residuals) in driving long-term temperature changes separately:

$$\frac{\partial \langle T \rangle}{\partial t} = AdvT + Q_H + RES \qquad [4]$$

Where AdvT is the contribution from both horizontal and vertical advection, Q_H the contribution from air-sea heat fluxes and Res is the term residual, comprising mixing processes and ε. The depth h was set to 110 m (or sea floor depth if shallower), which is deeper than the typical depth of the mixed layer in low-mid latitude coastal areas. The area A of integration was chosen as the OFAM3 horizontal grid cell, resulting in ~0.1°x0.1° area.

The computation of heat advection was done diagnostically using model outputs of the velocity vector and temperature and following the divergence theorem such as:

$$\mathrm{AdvT} = \frac{1}{V} \iiint^{V} -\mathrm{v.}\nabla T dV = \frac{1}{V} \iint^{S} -\mathrm{v.n} T dS \qquad [5]$$

Where **v** is the 3-dimensional velocity vector, S are the surfaces of the volume of interest and **n** is outward pointing normal unit vector to each surface. Given that the OFAM3 grid is orthogonal, the integral can be expanded to each face of the volume:

$$AdvT = \frac{1}{V} \left[\iint^{w} u_w T_w dydz - \iint^{e} u_e T_e dydz + \iint^{s} v_s T_s dxdz - \iint^{n} v_n T_n dxdz + \iint^{\mathrm{bot}} w_{\mathrm{bot}} T_{\mathrm{bot}} dxdy - \right.$$

Where n, s, w, e are the northern, southern, western and eastern face of the given orthogonal volume, respectively. The variable X_n therefore represents the spatial average of a variable X on the northern face.

To account for the internal heat redistribution processes expressed in individual directional elements of [6] which do not contribute to the volume-averaged temperature change, the Lee et al. (2004) method was adopted, yielding the final heat advection equation:

$$AdvT = \frac{1}{V} \left[\iint^{w} u_w (T_w - T) dydz - \iint^{e} u_e (T_e - T) dydz + \iint^{s} v_s (T_s - T) dxdz - \iint^{n} v_n (T_n - T) dxdz + \right.$$

Long-term trends

Datasets used in this study covered a common time-period of 33 years spanning Jan 1st 1982 to Dec 31st 2014. Long-term trends of a metric at a particular location were calculated from annual averages. A linear model was then fitted to the continuous yearly timeseries, from which the linear coefficient was defined as the long-term trend of the metric.

Applying a linear model to yearly temperature timeseries yields:

$$T(t) = \alpha t + b + \widetilde{T}(t) \qquad [8]$$

Where t is the time in years, α is the linear trend coefficient, b is the linear trend intercept and $\widetilde{T}$ are the residuals that are not explained by the linear trend. Combining [8] with [4], we get the following expression of the linear trend:

$$\alpha = \ AdvT + Q_T + Res - \frac{\partial \widetilde{T}}{\partial t} \qquad [9]$$

$$\alpha = \ \frac{1}{P}\left[\int \text{AdvT dt} + \int Q_T \text{ dt} + \int \text{Res dt} - \widetilde{T}\right] \qquad [10]$$

Where P is the number of years of the period used for the linear model and $\widetilde{T}$ is the temperature residual difference between the end and the beginning of the period. The term α is much smaller than most of the terms on the right-hand side of [10], as α is typically of the order of 1/10 degrees per year whereas heat budget terms can be up to hundreds of degrees per year. To manage this difference, [10] is applied to two distinct periods, named P_t and P_{ref}, where P_{ref} is not associated with significant temperature trends, and P_t captures the long-term temperature tendency (Y. Zhang et al., 2018).

$$\alpha_t - \alpha_{\text{ref}} = \ \langle \text{AdvT} \rangle_t - \langle \text{AdvT} \rangle_{\text{ref}} + \langle Q_T \rangle_t - \langle Q_T \rangle_{\text{ref}} + \langle \text{Res} \rangle_t - \langle \text{Res} \rangle_{\text{ref}}$$

Where $\langle - \rangle = \ \frac{1}{P}\int^t \text{dt}$ and α_{ref} is negligeable (non-significant long-term linear trend) relative to α_t.

Results & Discussion

Mean SST

The mean SST onshore-offshore difference shown in Figure 2 indicates that, on average, temperatures were colder onshore. The pattern has a clear geographic

distribution (Figure 2a) of cooler water onshore that is stronger in the mid-latitudes and weaker in the equatorial and southern latitudes. This pattern is robust and coherent across the ensemble mean onshore-offshore SST mean fields (Figure 2a). In the tropics, the mean SST difference is smaller. The difference is enhanced at mid-latitudes (~ 25°) where onshore temperatures were, on average, 1 degree colder than offshore. The highest difference was greater than 2 degrees and was observed along boundary current systems such as the Benguela Current or the Gulf Stream and on the Peruvian coast (Figure 2a). All upwelling and WBCs were associated with colder average SST onshore, except for the JS region (Figure 2a). The absence of a cross-shore gradient in this region can be explained by highly stratified waters, the warming effects of the Indonesian throughflow and the monsoon winds that drive the seasonality of local upwelling (Qu et al., 2005). The large seasonality of the SOM upwelling system (Chatterjee et al., 2019) can also explain the relatively weak onshore-offshore differences.

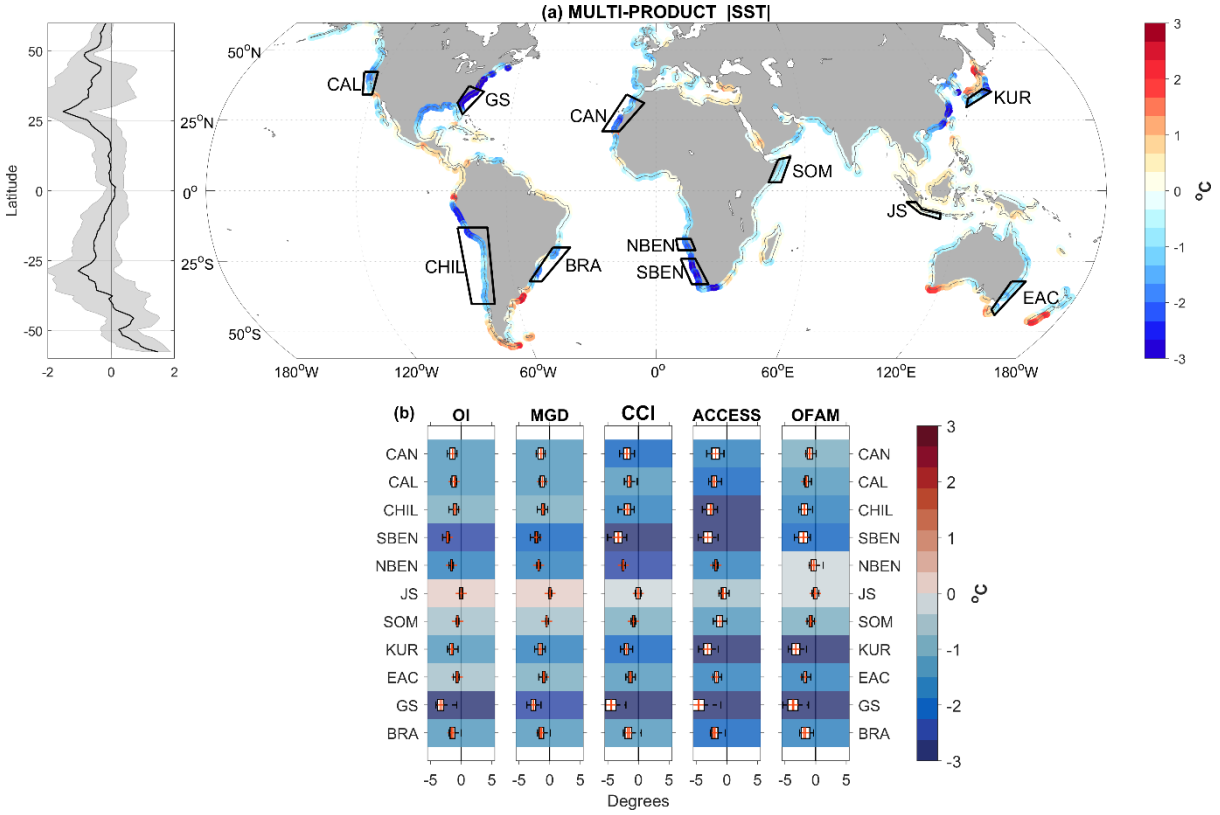

Figure 2: (a) Multi-Product mean of average SST difference between onshore and offshore pixels from 1982 to 2014. Running averages of pixels within 5-degree latitude bins are plotted in black. The grey shading indicates 1 standard deviation of values within each latitude bin. (b) Region boxplot of average SST difference between onshore and offshore pixels from 1982 to 2014. The mean (red

cross), median (red line) quartiles (blue) and 5th and 95th quantiles (grey) are plotted for each region. Shading highlights the mean value of the onshore-offshore difference with positive (negative) values shaded in red (blue).

Results from each individual product and model were box-averaged for all regions detailed in Table 1 to allow for easier comparison across observations, but also to assess model performance in these regions of interest (Figure 2b). There was a good agreement of mean SST differences between all observational products, highlighting the coherence of the cross-shore gradient of mean SST across all products. Both ACCESS and OFAM reproduced quite well observed SST gradient in sign and amplitude. The SBEN and GS regions were associated with the biggest SST difference of -3 and -4 degrees, respectively, across observations and models. We note that, contrary to ACCESS-OM2, OFAM does not fully resolve the onshore-offshore difference in the NBEN system. This upwelling system is notoriously difficult for models to simulate, which is largely due to the sensitivity to the representation of the local wind stress curl (Bonino et al., 2019; Small et al., 2015). Unlike JRA-55, the deterioration of wind-stress curl representation in favour of wind-stress speed and vector in ERA-Interim reanalysis could explain model differences in the NBEN system (Taboada et al., 2019).

SST trends

The difference of SST long-term trends between onshore and offshore pixels was globally negative across all observations (Figure 3). A negative difference indicates that onshore trends were smaller than offshore trends. Note that in the case of an offshore warming/cooling trend, a lower onshore trend indicates decreased warming/increased cooling. This signal was more pronounced along mid-latitude coastlines (Figure 3a-c). Regional averages showed that all upwelling regions were characterised by a lower onshore trend (Figure 3g). The onshore SST trend in WBC systems was also smaller than the offshore trend, except for the KUR and EAC regions in the OISST product. The onshore SST trend decrease was stronger in CCI, by ~0.1 degree per decade. The highest onshore-offshore difference was observed in the GS region where the onshore SST trend was 0.3-0.5 degrees per decade less than the offshore trend. We note that for some regions, there was no significant SST trend difference between onshore and offshore pixels (e.g., JS in both OISST and MGD).

This lower onshore trend contrasts with the warming trend that has been observed globally, including in coastal regions (Lima & Wethey, 2012). Positive onshore SST trends were observed in 7 out of the 11 regions including CAN, NBEN, JS, SOM, KUR, EAC and BRA. Thus, the negative onshore-offshore difference in SST trends indicates a dampening of the SST trend onshore compared to offshore (Figure 3). In those 7 regions of positive onshore SST trends, trends from CCI were weaker compared to OISST and MGD, which in turn explains the sharper onshore-offshore SST trend gradient observed in CCI. On the other hand, negative onshore SST trends were observed in CAL, CHIL and

GS across all products. Therefore, the onshore-offshore SST trend differences in the Pacific EBC regions and the GS are explained by an accelerated onshore cooling, contrasting with the global warming trends.

Our results were consistent with previous studies in highlighting a depressed nearshore warming along upwelling systems (Santos et al., 2012a; Santos et al., 2012b; Santos et al., 2016; Varela et al., 2016; Varela et al., 2018; Seabra et al., 2019). More importantly, our results were coherent across multiple SST satellite products, where previous studies only used the past version of NOAA OISST v2.1. This shows that the dampening of onshore SST trends is not attributable to the biases in the OISST product (Merchant et al., 2019) but is a clear and robust signal found in all of the SST products. Perhaps more remarkably, is that the lower onshore trends (i.e., supressed warming or accelerated cooling) are not only found in all upwelling systems included in this study, but extends to other coastal regions, including western boundary currents. 63.5 64 and 89 % of pixel pairs analysed were characterised by lower onshore trends in OISST, MGD and CCI respectively. The extension of this signal to a variety of coastal regions suggests that the driving mechanisms are not restricted to local physical processes of EBCs, but might instead be region specific.

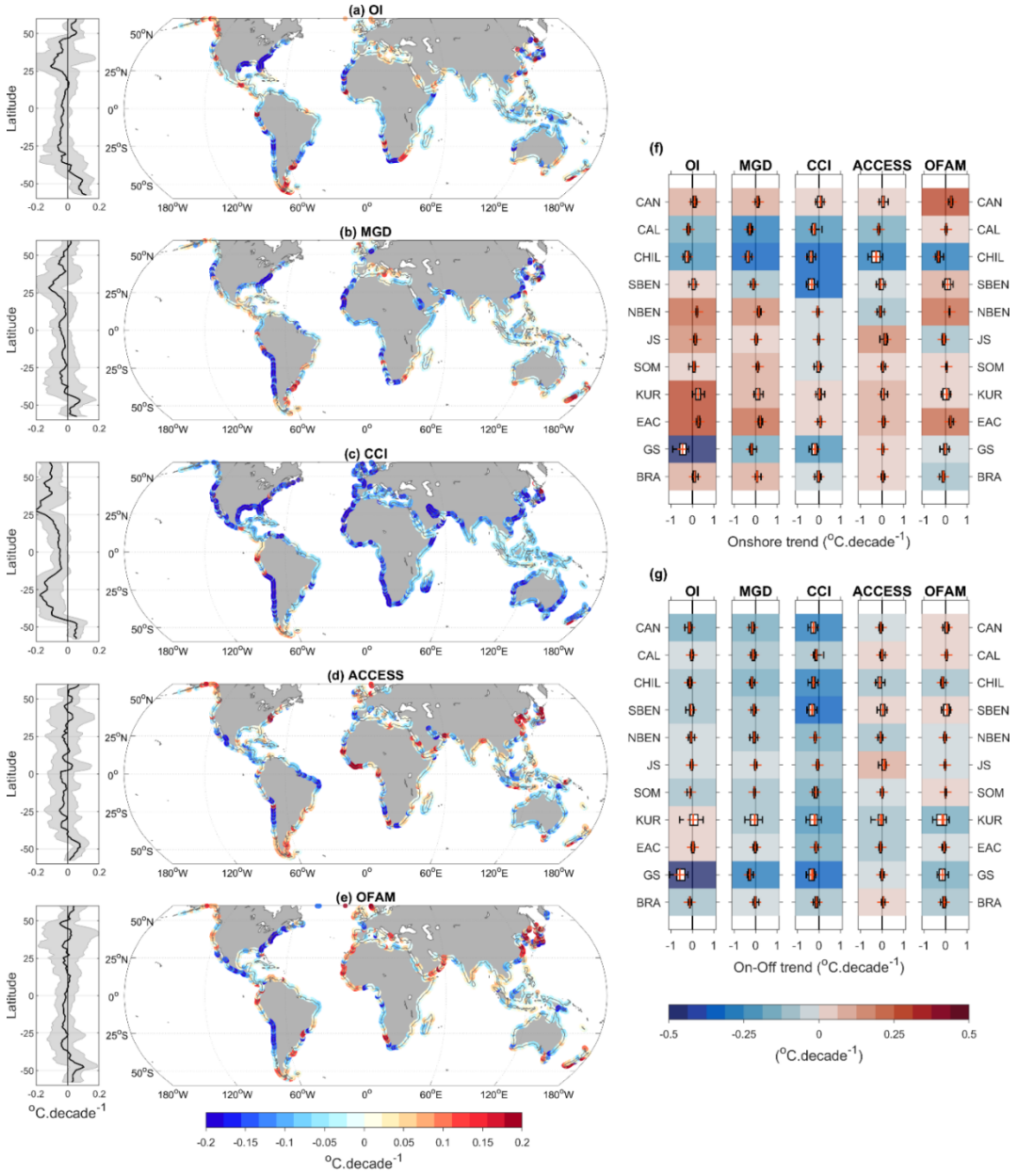

Figure 3: (a-e) Onshore-offshore differences of SST long-term trend derived from each product (maps). Running averages of pixels within 5-degree latitude bins are plotted (black curve). The grey shading indicates 1 standard deviation of values within each latitude bin. Region boxplot of (f) onshore and (g) onshore-offshore SST long-term trends. The mean (red cross), median (red line) quar-

tiles (blue) and 5th and 95th quantiles (grey) are plotted for each region. Shading highlights the mean value of the onshore-offshore difference with positive (negative) values shaded in red (blue).

Comparisons of OFAM3 and ACCESS-OM2 with observations revealed that neither model captured the global lower onshore SST trend as found in observations (Figure 3d and 3e and 3g). Modelled onshore-offshore SST trend differences were smaller than observed in upwelling systems (Figure 3g), with the exception of the CHIL region where SST trend differences of ~-0.1 degrees were observed in both models. The strong onshore accelerated cooling observed in the CHIL region was therefore also captured in the models. In NBEN, a negative trend difference was observed in ACCESS-OM2 but the onshore SST trend did not compare well with observations (Figure 3g). Based on these results, the models' difficulties in representing wind-driven upwelling systems are likely to affect, in part, the ability of these models to accurately represent SST trends in forecasts and projections of climate change.

Mean Marine Heat Wave Metrics

Average MHW metric difference between onshore and offshore locations were also investigated for each data product. Figure 4 shows the onshore-offshore difference of average annual MHW exposure (MHW Days) and yearly cumulative intensity (YCI) for every onshore-offshore pair and region averages. There were little differences between onshore and offshore MHW days in MGD (Figure 4b). The onshore-offshore gradient increased in OISST to 2 to 3 MHW days per year, but the global distribution had no clear relationship with latitude (Figure 4a). In contrast, CCI showed strong differences between onshore and offshore, especially in the 25°S to 25°N tropical band (Figure 4c). There were on average 4-5 more MHW days per year in coastal pixels compared to offshore. This increase is significant when compared to CCI annual MHW exposure in the tropics, estimated to range between 20-30 days per year at the onshore pixel (Marin et al., 2021). ACCESS showed a smaller increase of MHW exposure towards the coast restricted to some tropical regions including the maritime continent, north-western Indian Ocean and equatorial Atlantic Ocean (Figure 4d). OFAM3, in contrast, showed no tropical enhancement of onshore MHW exposure. ACCESS-OM2 and OFAM3 both showed fewer MHW days per year onshore than offshore at higher latitudes, especially in the southern hemisphere (Figure 4d and 4e). This was illustrated by fewer MHW days in all EBCs for both models, despite observations showing small/positive differences (Figure 4k).

Onshore-offshore differences in YCI were more consistent amongst observations than MHW days. Differences were most significant in mid-latitudes (25°), especially along EBCs (Figure 4f and 4h). On average, onshore YCI was 10-20°C.days higher than offshore, across all observations. This was consistent for all upwelling regions (Figure 4l). Significant positive onshore-offshore differences were observed in the Atlantic WBC regions, with similar amplitudes as

EBCs. The only onshore decrease in mean YCI was observed in the EAC region. Both OISST and MGD showed no significant YCI differences in the tropics nor in high latitudes. However, slightly smaller YCI values were observed onshore compared to offshore in CCI in the tropics and high latitudes (Figure 4h). Unlike MHW exposure, both models compared well with observations for average YCI differences (Figure 4i and 4j). A similar positive difference in mid-latitudes was observed, corresponding to increased onshore average YCI in all EBC regions (Figure 4l). Models also captured smaller onshore average YCI values in the EAC. We note that models slightly overestimated the amplitude of the difference in the CHIL, EAC and GS regions.

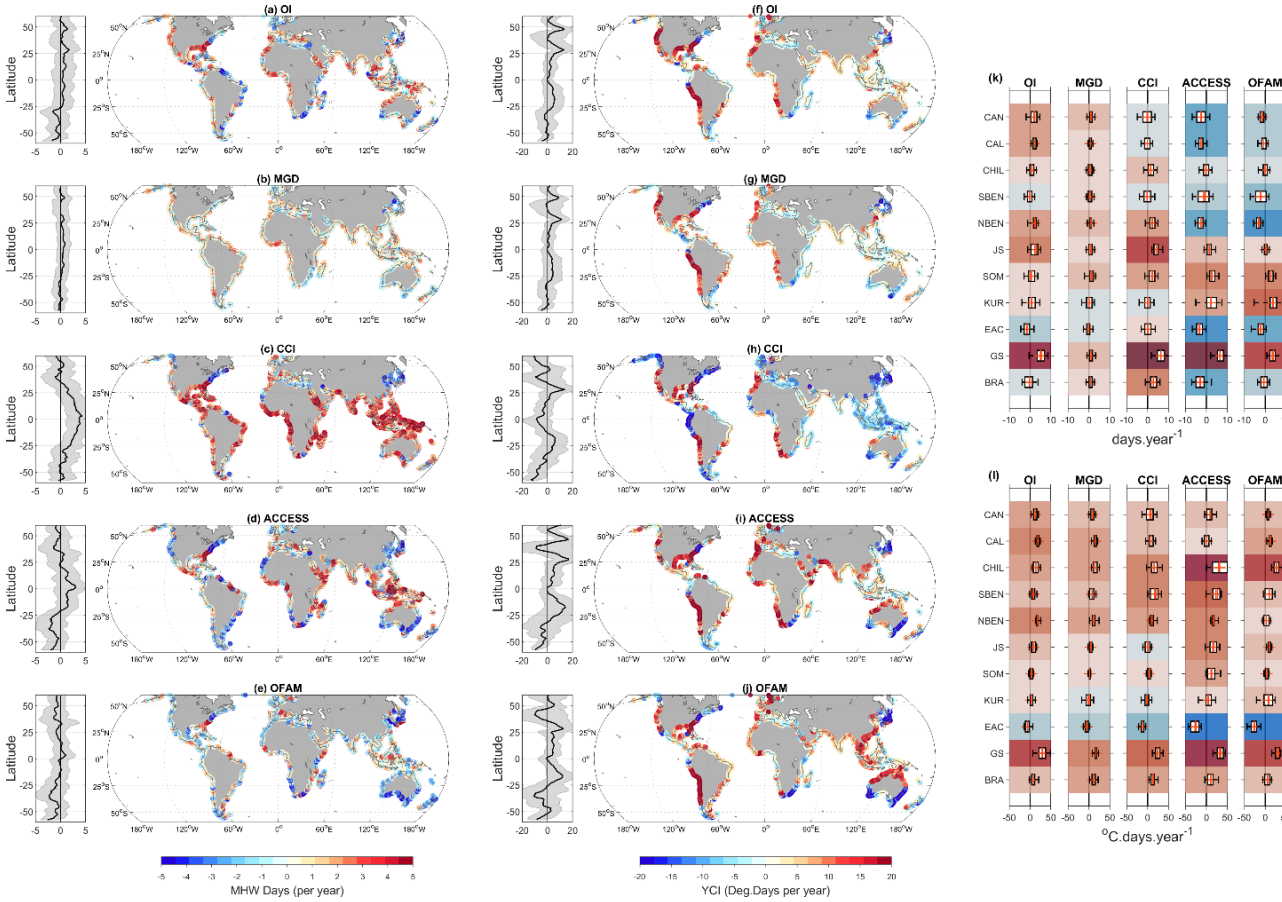

ure 4: Average MHW metric differences between onshore and offshore pixels. (a-e) annual MHW days and (f-j) yearly cumulative intensity differences are plotted for each product. Running averages of pixels in 5-degree latitude bins are plotted in black. The grey shading indicates 1 standard deviation of values within each latitude bin. Positive indicates onshore pixel has higher MHW exposure. Region boxplot of onshore-offshore mean (k) annual MHW days and (l) yearly cumulative intensity during 1982-2014. The mean (red cross), median

(red line) quartiles (blue) and 5th and 95th quantiles (grey) are plotted for each region. Shading highlights the mean value of the onshore-offshore difference with positive (negative) values shaded in red (blue)

Cumulative MHW metrics were found to compare better amongst different satellite observations than "basic" metrics such as frequency, duration or intensity (Marin et al., 2021). YCI combines all MHW basic metrics. There are clear differences in frequency, duration and intensity across all products (Figure S1). These biases can be attributed to differences in spatial and temporal resolution, instrumentation (microwave vs infrared), calibration, or properties of algorithms converting satellite measurements to temperature at a specific depth (Beggs, 2019; Marin et al., 2021). The resulting varying statistical properties of timeseries (Fiedler et al., 2019) in turn create important biases in MHW statistics (Oliver, 2019; Oliver et al., 2021). Unlike this study, Marin et al. (2021) did not find significant differences of average coastal MHW days across a range of SST observations including OISST, MGD and CCI. The authors used a detrended climatology for their MHW identification to better quantify the impact of long-term changes in SST. This greatly increased values of average MHW statistics, explaining the decreased multi-product spread. Further work is needed to better understand how timeseries properties influence MHW properties and what differences can be expected depending on the product of choice. Nevertheless, our results show a consistent coherence of cumulative metrics such as YCI across observations and models. This encourages their use in predictive studies as well as investigations of the sensitivity of ecosystems to MHWs. Ecosystems and biota respond differently to different threshold and metrics, and both long-term press and pulse changes of climate trends are equally as important in driving biological responses (Harris et al., 2018). Cumulative metrics capture all aspects of extreme events, but also carry the signature of long-term changes of the climate system, being more appropriate for ecosystem management analysis and decisions.

Trends in MHW metrics

Global onshore-offshore differences of trends in MHW exposure and YCI are presented in Figure 5. There was an overall lower MHW exposure trend onshore than offshore in OISST and MGD, with the exception of high latitudes in the southern hemisphere (Figure 5a & 5b). CCI differed again from the two other products in the tropics, where trends in MHW days were higher onshore than offshore (Figure 5c). The pattern of YCI trend difference was similar to that of MHW days. There was a global reduction of YCI trends onshore, especially in EBC upwelling systems, as reflected by the region boxplots (Figure 5l). The lower onshore trends of both MHW days and YCI in EBC regions were consistent across observations, ranging from -2 to -10 MHW days per decade and -2.5 to -15°C.days per decade, respectively, depending on the region. Within EBC boxes, highest differences of MHW days trends were observed in the CAN region, where the onshore trend was 6 MHW days per decade less than offshore. The highest

differences of YCI trends were observed in the CHIL region, especially in CCI, as onshore trends were more than 10°C.days.year per decade lower than offshore. We note that the highest onshore-offshore differences observed across all regions studied were in the GS region for OISST and MGD (i.e., -20 MHW days per decade and -40°C.days.year per decade, respectively).

Our results are consistent with Varela et al. (2021), where the authors used NOAA OISST 2.0 data to identify depressed onshore trends of MHW days by -8.01,-5.63,-6.96 and -8.9 days per decade for the Benguela, Canary, Chile and California coast respectively. Despite minor differences in region coordinates, offshore pixel identification and period of calculation (Varela et al. focused on 1982-2018), we confirmed the lower onshore MHW exposure trends in OISST but also using different SST products (product average of -3.79, -5.32, -9.66, -5.42, -4.73 MHW days per decade in NBEN, SBEN, CAN, CHIL and CAL respectively). This increases our confidence in the results suggesting that upwelling systems act to dampen the global increasing MHW trends, or in some regions like the eastern Pacific, enhance a decrease in MHW trends during the past decades (Frölicher et al., 2018; Marin et al., 2021; Oliver et al., 2018).

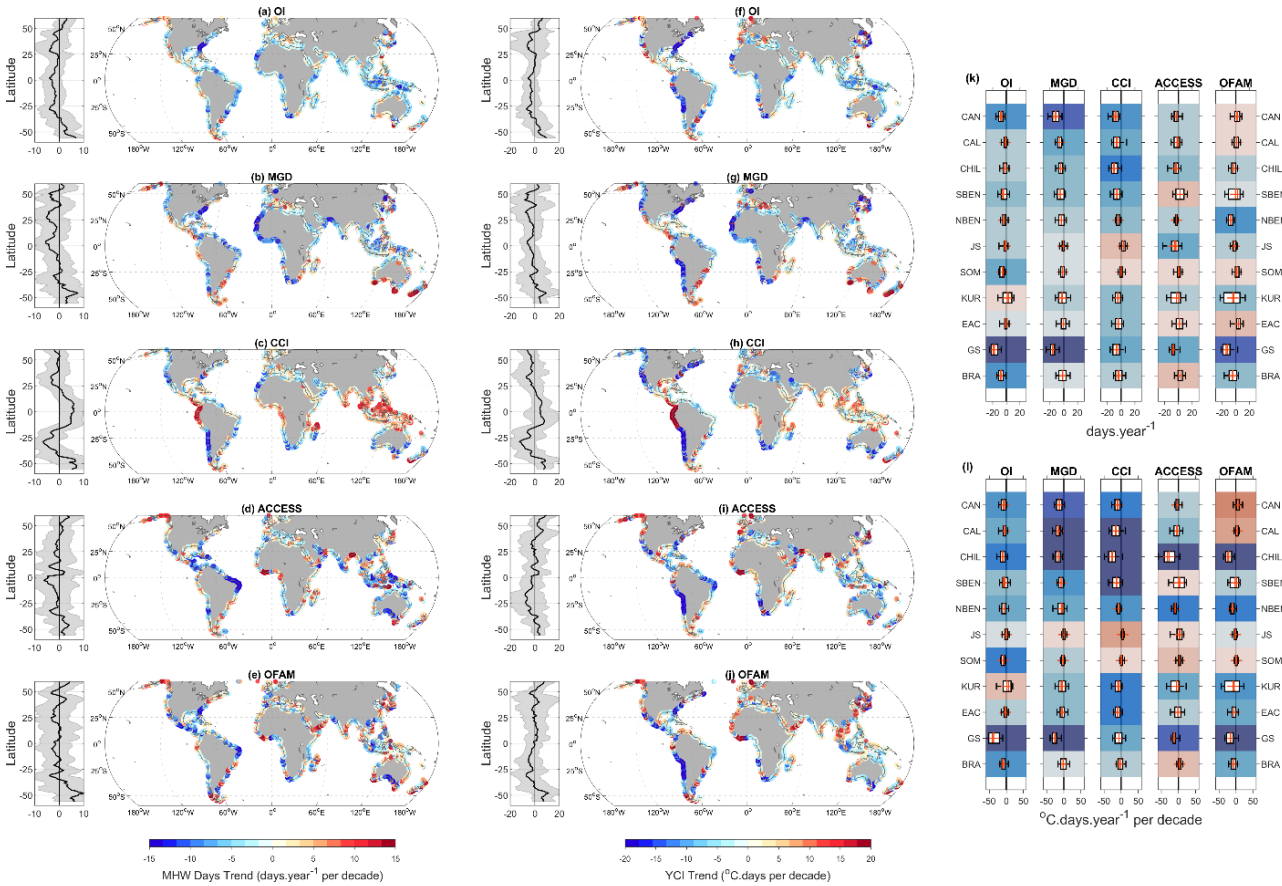

ure 5: Same as Figure 4 for long-term trends.

Neither model captured the lower onshore trends of MHW days and YCI (Figure 5i-j) which was evident in observations. However, the models performed reasonably well in individual regions such as CHIL, NBEN and GS, especially for YCI trends. Note that models were in closer agreement in WBC regions compared to upwelling regions (Figure 5l). This suggests that the limited ability of models to correctly capture SST and MHW variability stems from issues inherent to global ocean models. At a resolution of 0.1°, numerical models are still challenged to capture large scale, interannual variability and important mesoscale processes, prominent in coastal areas, that affect SST patterns and in turn, MHW representation (Hayashida et al., 2020; Pilo et al., 2019).

Impact of Long-term SST change on MHW trends

As long-term SST change was described as the main forcing of MHW trends both in the global ocean (Oliver, 2019) and in coastal areas (Marin et al., 2021), we investigated the importance of this relationship for cross-shore gradients. Figure 6 shows the linear correlations of long-term SST and MHW trends differences between onshore and offshore locations. Significant positive correlations were found for both the OISST and MGD products. YCI trend differences were slightly better correlated ($R^2 = 0.95$ and $R^2 = 0.91$ for OISST and MGD, respectively) than MHW days ($R^2 = 0.9$ and $R^2 = 0.83$ for OISST and MGD, respectively). This indicates that lower onshore MHW trends are associated with the decreased onshore trends. Past studies have indicated that long-term changes in the mean SST were the main driver of observed MHW trends (Oliver et al., 2018, Marin et al., 2021). However, in some regions such as the eastern Pacific Ocean, internal variability was the main contributor of the observed decrease of MHW metrics during the past decades. Here, results suggest that differences in long-term changes of MHWs between onshore and offshore locations in Pacific EBCs (i.e., CAL and CHIL) are well correlated with differences in long-term SST changes (Figure 6). The SST anomaly signature of El Nino Southern Oscillation (ENSO), the main driver of inter-annual variability in the eastern Pacific, is arguably homogeneous along coastal regions, spreading further offshore than 150km. Therefore, long-term changes in ENSO would have a limited influence on the cross-shore gradient of SST changes.

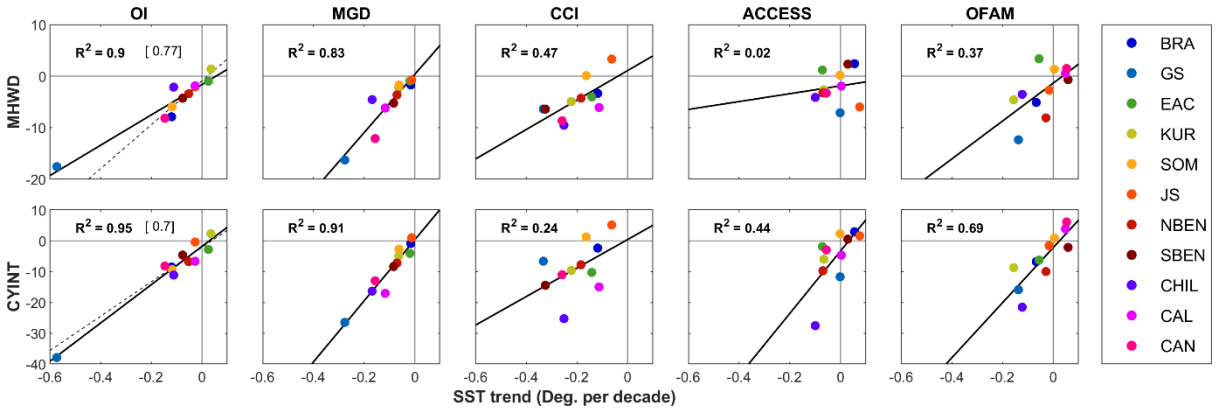

Figure 6: Scatterplots of regionally averaged onshore-offshore SST trend difference to MHW days (days per decade, top row) and yearly cumulative intensity (°C.days per decade, bottom row) trend difference during 1982-2014. Each point represents the mean of one specific region (11 regions in total). The black line was derived from a linear regression, with corresponding R^2 values indicated on each panel. Secondary linear regressions (dashed line) were computed after removal of the Gulf Stream region outlier for the OISST product. The corresponding R^2 value is indicated by the number in brackets.

The CCI correlations between SST and MHW trend differences were weaker than OISST and MGD. MHW days were better correlated ($R^2 = 0.47$) than YCI ($R^2 = 0.24$) with SST trend differences. Nevertheless, all regions in CCI, to the exception of SOM and JS, were associated with negative trend differences in MHW metrics and SST (Figure 6). One feature of the CCI product is that, unlike most other Level-4 (daily global gap-free) satellite products, it does not include assimilation of in-situ observations, which is important to correct the cold bias of infrared measurements due to cloud cover (Marquis et al., 2017). Further work is needed to quantify the effects of a lack of data assimilation on long-term trend derivations.

Despite the limited ability of models to capture the dampened SST (Figure 7) and MHW trends (Figure 8), there was a moderate correlation of YCI trend differences with SST trends in both models ($R^2 = 0.44$ and $R^2 = 0.69$ for ACCESS-OM2 and OFAM3, respectively). The correlation of SST with MHW exposure was less evident than with YCI in both models, as ACCESS-OM2 failed to capture any correlation ($R^2 = 0.02$ and $R^2 = 0.37$ for ACCESS-OM2 and OFAM3, respectively).

Drivers of long-term SST trends

Atmospheric drivers

Long-term trends of air-sea heat fluxes and surface winds were computed to investigate the drivers of the depressed onshore SST trend. The onshore net

air-sea heat flux has globally decreased during 1982-2014, indicating a reduction of heat transfer from the atmosphere to the ocean (Figure 7a). The main contributor of the onshore decrease of air-sea heat flux was an increase in latent heat cooling (Figure 7g). A decrease in incoming short-wave radiation in the tropics contributed to the net decrease (Figure 7c), while longwave radiation and sensible heat contributions were negligeable. The onshore-offshore differences of net air-sea heat flux were mostly positive, suggesting a stronger reduction of air-sea heat flux heating offshore (Figure 7b). Latent heat was the only significant contributor to the cross-shore trend differences, as onshore shortwave radiation trends were similar to offshore (Figure 7d). The increased offshore evaporative cooling trend is surprising given the increased offshore SST warming (or reduced cooling; Figure 3). This suggests that the smaller reduction in net/latent heat flux to the ocean onshore relative to offshore is likely a response to the depressed SST trends onshore. Indeed, an onshore reduced warming/increased cooling decreases its heat content relative to offshore, which in turn decreases the amount of heat loss due to evaporation. Nevertheless, negative onshore-offshore differences of net air-sea heat flux (towards the ocean) trends was associated to lower onshore SST trends in 22, 19 and 20% of cases for OISST, MGD and CCI respectively (Figure 7a). This indicates that air-sea heat flux might, locally, be able to explain the lower onshore SST trends.

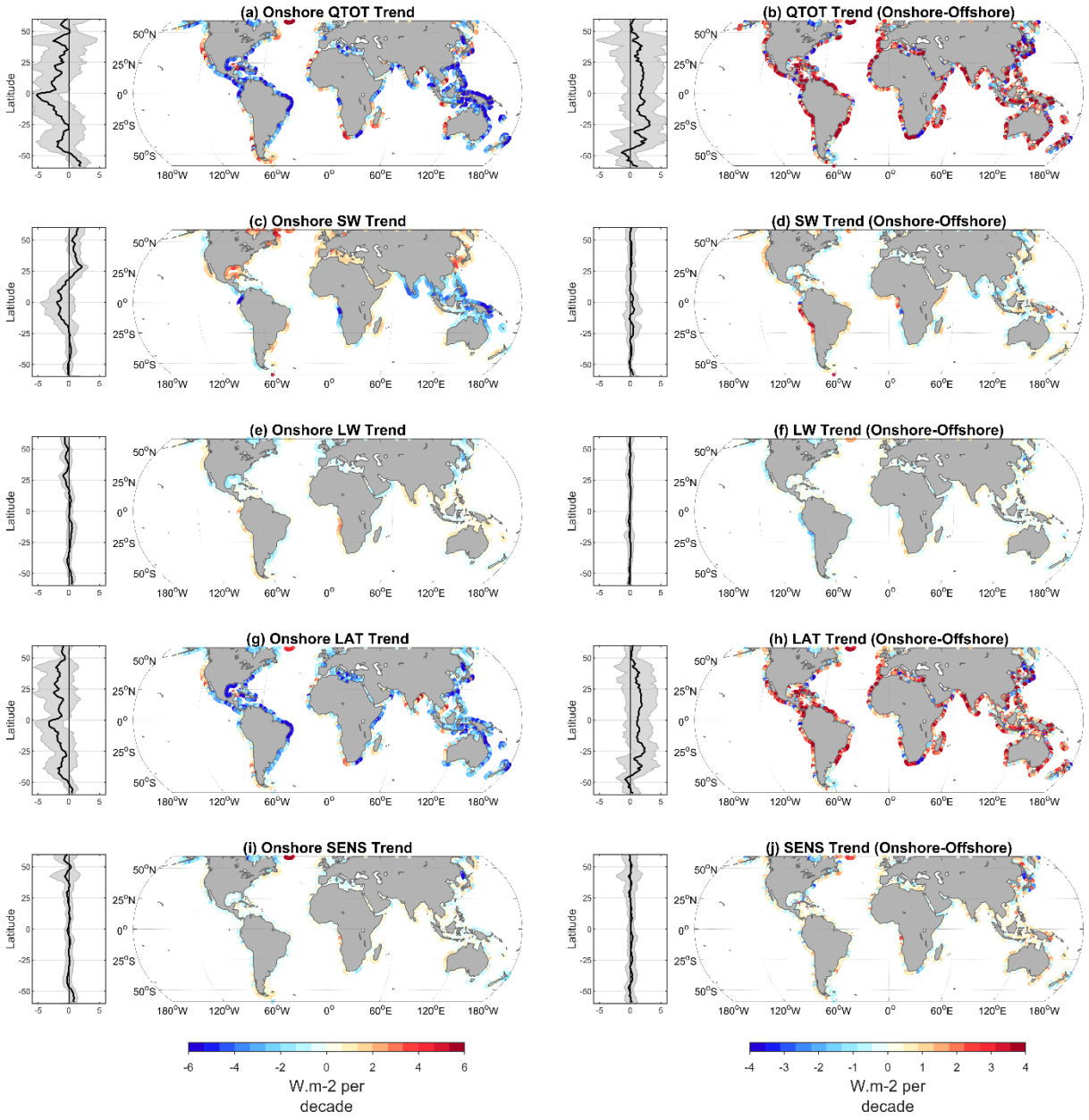

Figure 7: Heat Fluxes long-term trend (1982-2014) and onshore-offshore differences derived from ERA5. (a-b) Total net air-sea heat flux, (c-d) surface shortwave radiation, (e-f) longwave radiation, (g-h) latent and (i-j) sensible heat fluxes are plotted separately. Positive values are heating the ocean. Running averages of pixels within a 5-degree latitude bin are plotted (black curve). The grey shading indicates 1 standard deviation of values within each latitudinal band.

Analyses of wind speed trends highlighted a global pattern of onshore decrease of wind speeds compared to offshore (Figure 8b), consistent with an onshore reduction of evaporative heat loss. The highest differences were observed in the CAL region where onshore wind speed trends were 0.2m.s^{-1} per decade lower than offshore (Figure 8d). The onshore wind speed trends of -0.25m.s^{-1} per decade (Figure 8c) observed in the CAL region indicates that the negative wind speed trends were restricted near-shore. In contrast, weak onshore wind speed trends in the GS and BRA region were accompanied with significant positive offshore trends (negative onshore-offshore difference). Several studies have attributed a global decrease of terrestrial surface wind speeds to an increase in land frictional forces (Wu et al., 2018; Z. Zhang et al., 2019), explaining the gradient of wind speed changes between onshore and offshore pixels.

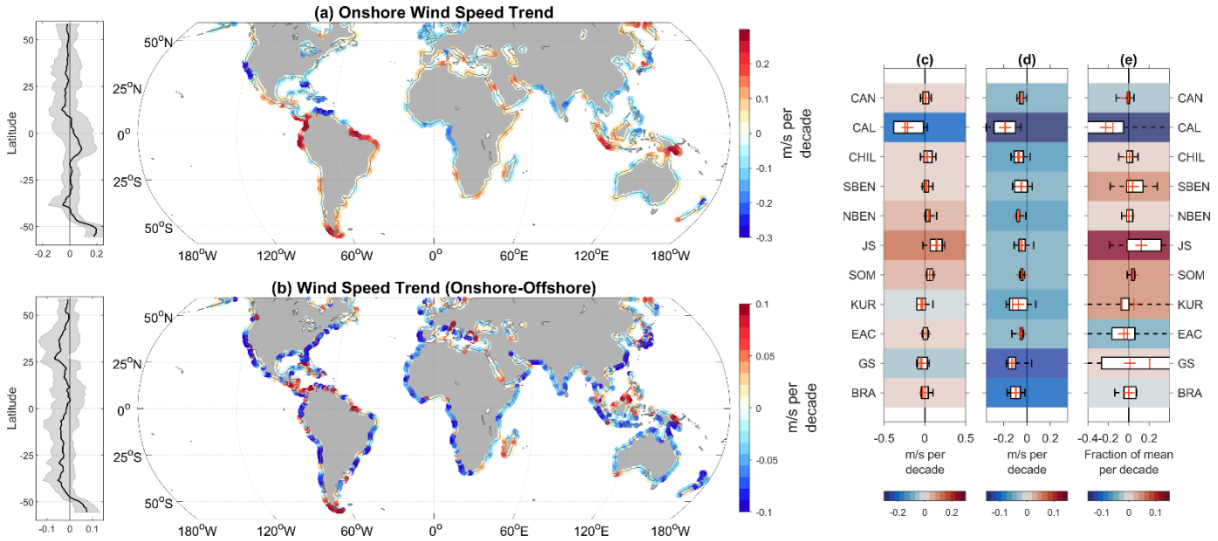

Figure 8: (a) ERA-Interim mean annual wind speed long-term trends. (b) Mean annual wind speed long-term trend differences between onshore and offshore pixels. Running averages of pixels within a 5-degree latitude bin are plotted (black curve). The grey shading indicates 1 standard deviation of values within each latitudinal band. Region boxplot of (c) onshore wind speed trends, (d) onshore-offshore difference of wind speed trends and (e) onshore Ekman transport trends as a fraction of the mean annual transport per decade. All long-term trends were calculated from 1982-2014. The mean (red cross), median (red line) quartiles (blue) and 5th and 95th quantiles (grey) are plotted for each region. Shading of region boxes highlights the mean value, with positive (negative) values shaded in red (blue).

In most of the 7 upwelling regions, offshore Ekman transport trends derived from alongshore winds at onshore pixels were positive, excluding CAL and CAN (Figure 8e), corresponding to an increase in upwelling (0.5%, 3.8%, 0.02%, 12.3% and 4% per decade for CHIL, SBEN, NBEN, JS and SOM, respectively). In-

creases in upwelling can be explained by increases of near-shore wind speeds in most regions (Figure 8c), despite onshore pixels showing a smaller trend than offshore. Major coastal upwelling systems are influenced by alongshore winds in a large coastal band, that is likely to extend as far as the offshore cell (~150km away from the coast). An intensification of upwelling supports depressed onshore SST trends. Both were observed coincidently in 53, 58 and 60 % of pixels within EBC regions for OISST, MGD and CCI respectively. However, our results indicated that upwelling at CAN and CAL has been decreasing during 1982-2014 (Figure 8e). The significant decrease of upwelling in the CAL region was associated with a sharp decrease of onshore wind speed (Figure 8c). A weakening of upwelling should result in an onshore warming, which was not observed in the CAL region (Figure 3g), suggesting that the decrease in upwelling was not the main driver of temperature trends in this region. The positive trends of offshore Ekman transport in the CHIL and NBEN systems were not significant. The uncertainty of long-term changes in upwelling intensity is demonstrated by conflicting results from past research. For example, although our results indicate a strong decrease in upwelling in the CAL region, the contrary has been shown in other studies (Patti et al., 2010; Rykaczewski & Checkley, 2008). These discrepancies have been attributed to several factors, including the choice of region coordinates, period of study and dataset (García-Reyes & Largier, 2010; Narayan et al., 2010; Seo et al., 2012; Sydeman et al., 2014; Varela et al., 2015), and are common for most upwelling systems to the exception of the Benguela region (Varela et al., 2015).

Despite clear evidence that reduced onshore SST trends and resulting reduced onshore MHW trends are associated, in part, with upwelling systems, further work is needed to better quantify changes in upwelling and its associated impact on SST trends. Moreover, our results highlighted that the onshore decrease of SST trends and lower MHW trends were not restricted to upwelling regions (Figure 3 and 5). This highly suggests that processes controlling such cross-shore differences vary on a regional scale. While changes in upwelling can explain a lower onshore SST trend in the South-Benguela, Java-Sumatra and Somalia upwelling systems, the relationship did not hold in other regions, including EBC systems.

Heat Budget Analysis

One of the most convenient way to investigate changes in temperature is via a heat budget analysis. This allows for a comprehensive quantification of terms regulating changes of temperature. It can be especially useful in WBC systems where the dampened trend could not be explained by either heat fluxes or offshore Ekman transport. To illustrate this, a monthly heat budget analysis was computed for the CHIL using OFAM3 outputs. Those regions were chosen as OFAM3 (and ACCESS-OM2) successfully captured a depressed onshore SST trend (Figure 3g). The 0-110m integrated temperature trends were similar to SST trends in this region, justifying the use of the 0-110m integrated budget to investigate the drivers of SST trends (not shown).

The yearly heat budget averaged over 1982-2014 indicated that the major contributors of yearly 0-110m depth-averaged temperature (referred to temperatures thereafter) change were advection and net air-sea heat flux at both onshore and offshore locations (Figure 9a and 9d). The value of yearly heat budget terms was almost an order of magnitude larger onshore. Total advection typically acted to remove heat from the system while net-air sea heat fluxes added heat to the system. Vertical heat advection largely dominated horizontal heat advection (Figure 9b and 9e), coherent with the strong coastal upwelling associated with the CHIL region. Shortwave radiation was the dominant and only positive heat flux term both onshore and offshore (Figure 9c and 9f).

Timeseries of annual temperature means revealed that a period of relatively weak warming from 1982 to 1992 preceded a significant cooling which was captured by the long-term trends (Figure 9a). This period of weak warming was selected as P_{ref}. The 1992-2014 cooling was enhanced onshore (-0.63°C per decade) compared to offshore (- 0.46°C per decade), resulting in the negative onshore-offshore difference reflected in observations (Figure 3). Importantly, the onshore and offshore temperature trends during Pref were identical.

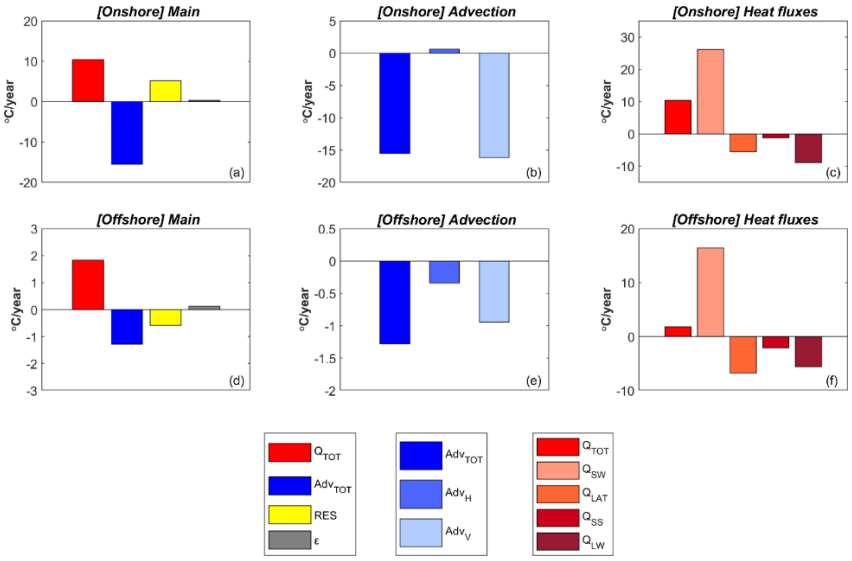

Figure 9: Mean 0-110m heat budget at the CHIL region. Average yearly heat budget terms (°C.year^{-1}) for the period 1982-2014 at (a) onshore and (d) offshore pixel. Q_{TOT} (red) is the net air-sea heat flux term, Adv_{TOT} (blue) is the total advection term, RES (yellow) is the non-advective ocean processes term and (grey) is the residual term. (b,e) decomposition of the advection term into its horizontal (Adv_H) and vertical (Adv_V) components. (c,f) decomposition of the net air-sea heat flux term into turbulent (sensible and latent heat fluxes, denoted Q_{SS} and Q_{LAT}, respectively) and radiative heat fluxes (downward shortwave and longwave radiation, denoted Q_{SW} and Q_{LW}, respectively). Note the difference in y-axis scale between onshore and offshore pixels.

Results from the heat budget difference between P_t and P_{ref} indicated that negative trends were largely driven by an increase in advective cooling at both onshore and offshore locations (Figure 10b and 10e). All remaining terms had positive contributions to long term temperature changes. Net air-sea heat flux was the dominant warming term offshore while non advective ocean processes added the most heat onshore. Despite being the main driver of the local trend, advection had a minor contribution in driving the negative onshore-offshore temperature trend difference (Figure 10h). The advective cooling was similar at onshore and offshore locations. Rather, the difference of net air-sea heat fluxes was the only negative term. The increased warming from net air-sea heat fluxes offshore (Figure 10e) did not occur onshore (Figure 10b), resulting in a stronger onshore cooling. Non-advective ocean processes had a significant warming contribution, opposing the increased onshore cooling, but its absolute value remained smaller than the cooling contribution from air-sea heat fluxes (Figure 10h). The decomposition of the net air-sea heat fluxes term showed that longwave radiations were the main driver of the increased onshore cooling (Figure 10j). The offshore contribution of longwave radiations in long-term temperature changes was weak (Figure 10g), whereas it had a significant cooling effect on onshore temperatures (Figure 10d). A significant increased warming from shortwave radiations acted against the increased longwave radiative cooling at onshore locations, but its difference with offshore locations remained smaller, resulting in the overall positive contribution of air-sea heat fluxes to the accelerated onshore cooling relative to offshore.

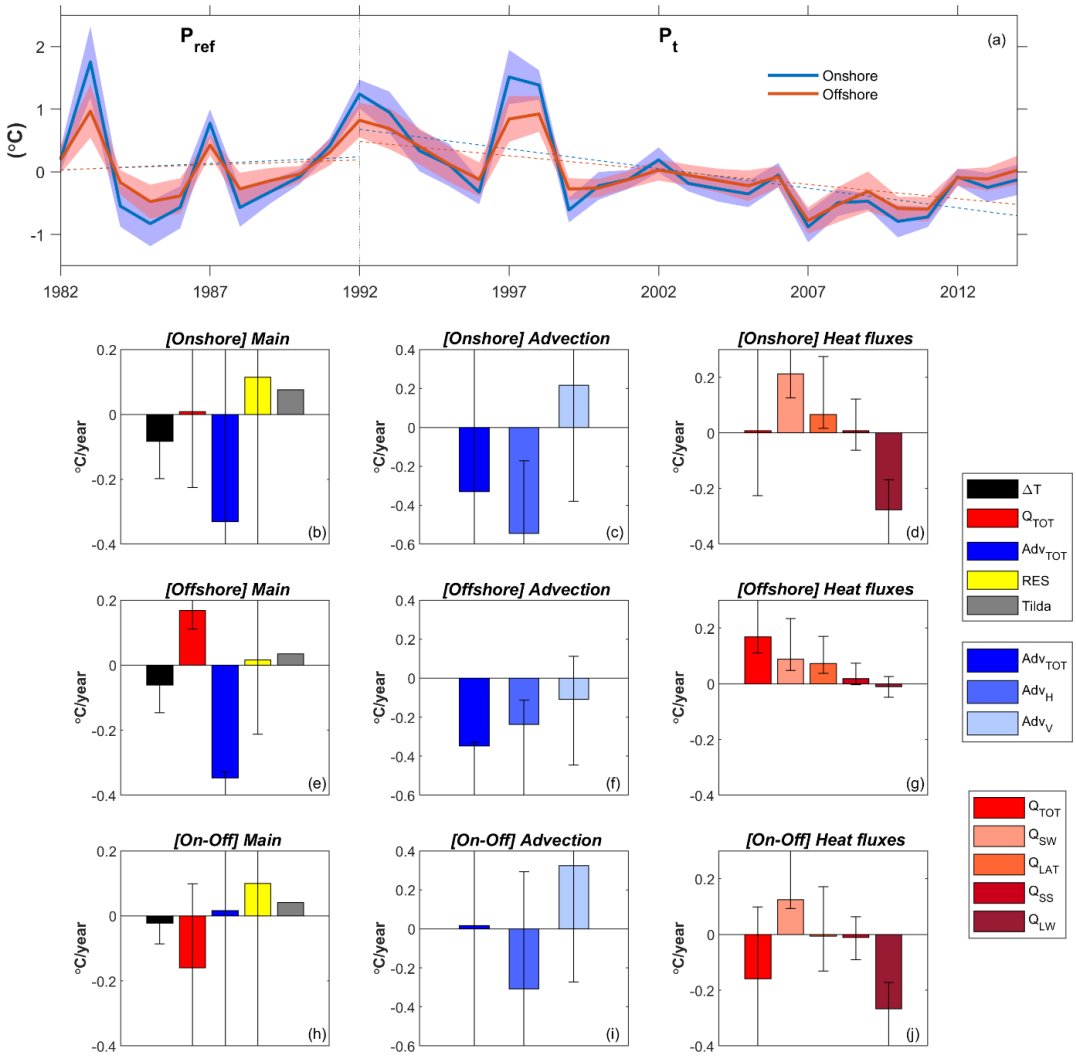

Figure 10: Heat budget analysis of temperature long-term trends in the Chilean region. (a) Timeseries of yearly mean 0-110m depth averaged temperature anomalies of the Chilean region. The thick lines depict the onshore (blue) and offshore (red) pixel's average for the region, and its standard error (shaded). P_{ref} define a period where there is no long-term change in temperature. P_t define a period of significant long-term change in temperature. Linear trends of individual periods are shown by the dashed line. The $P_t - P_{\text{ref}}$ difference of mean annual heat budget terms are plotted for (b) onshore, (e) offshore and (h) onshore-offshore pixels' average. ΔT (black) represents the mean annual temperature change difference between P_t and P_{ref} due to the linear trend. The contribution from (red) net air-sea heat flux, (blue) advection, and (yellow) remaining ocean processes to the linear trend difference (see [11]) are indicated by the remaining

bars. The grey bar (Tilda) indicates the mean annual temperature change that is not captured by the linear trend. The relative contribution of (c,f,i) horizontal and vertical advection to total advection and (d,g,j) turbulent (sensible and latent heat fluxes, denoted Q_{SS} and Q_{LAT}, respectively) and radiative heat fluxes (downward shortwave and longwave radiation, denoted Q_{SW} and Q_{LW}, respectively) to the total heat flux are also plotted. The 1^{st} and 3^{rd} quartile of budget terms from individual pixels included in the region are indicated by the error bars for each budget term.

Net surface longwave radiation is a balance between downward longwave radiation and upward longwave radiation. Downward longwave radiation is a direct measure of radiative warming of the surface by the lower atmosphere and highly depends on the concentrations of various greenhouse gases and aerosols (Liang, 2017). Upward longwave radiation is the addition of reflected downward longwave radiation by the surface and emission of thermal longwave radiation by surface cooling. Therefore, the increased net longwave radiative cooling is likely due to a decrease in downward longwave radiation, as decreasing SSTs reduce upward longwave radiative emission/cooling. Despite a global increase in cloud cover, it has been shown that in some regions like the south-west coast of South America, there has been a decrease in precipitation and cloud cover in the last few decades (Dewitte & Clerbaux, (2018), Figure 5). A decrease in cloud cover is consistent with a decrease in downward longwave radiation and reflects the onshore increase in shortwave radiation (Figure 10). Moreover, outputs from ERA-Interim reanalysis, whose radiative fluxes were used to force OFAM3, showed a negative onshore-offshore difference in cloud cover trends, indicative of an intensified decrease of cloud cover in the coast (Figure S8). Nevertheless, mechanisms controlling the variability of downward longwave radiation remain complex and would require further investigation.

We note that there was no increase of vertical advective cooling onshore. The Bakun (1990) theory implies an increase of vertical advective cooling via increased upwelling. Such an increase was observed offshore but remained smaller than the cooling contribution of horizontal advection (Figure 10f). Although ERA-Interim winds captured an increase in long-term onshore wind speed (Figure 8c) along the CHIL coast, resulting in a 0.5% increase in offshore Ekman transport per decade, the ability of the model to properly resolve upwelling at coastal cells remains uncertain. It is possible that the model therefore compensated with an increase in horizontal advection cooling, consistent with increased wind stress.

Conclusion

Here, we provide a comprehensive analysis of the difference of changes in SST and MHWs between the coast and offshore regions, using a combination of satellite SST observations and OGCMs. Our results confirm that most coastal regions are associated with depressed SST trends during the past decades, reveal-

ing a coastal dampening of global warming trends. These SST trend differences drove similar depressed trends of MHW metrics along the coast. More importantly perhaps, our study shows that this was consistent across multiple satellite SST products, when previous studies restricted their analysis to a single product (Varela et al., 2016; Varela et al., 2018; Seabra et al., 2019). Therefore, there is increased confidence that coastal regions can act as potential thermal refugia for ecosystems being under increasing thermal stress in the context of global warming. Not only is long-term warming mitigated near-shore, but exposure from risks associated with higher frequency extreme events (I.e., marine heatwaves) is also reduced.

The signal of depressed SST trends was not only restricted to upwelling regions; depressed onshore trends were not primarily driven by changes (i.e., increases) in coastal upwelling. Even within upwelling regions, there were no systematic increases in upwelling transport, suggesting that the identification of processes controlling the cross-shore gradient of long-term changes requires a more complex analysis. Ocean models, via heat budget analysis, are necessary tools that can provide better insights of terms contributing to temperature changes. Although models captured, to some extent, the relationship between the difference of long-term changes in SST and MHWs between onshore and offshore locations, they were not able to reproduce the sign of the difference consistently. In the case of the Chilean region, where models were able to capture depressed onshore trends, a stronger decrease of downward longwave radiation was identified as the main source of lower coastal trends, despite model forcings capturing an increase of upwelling favourable winds. This surprising result speaks to the difficulty of ocean and climate models to accurately resolve small scale coastal processes, including ocean-atmosphere feedbacks, exacerbated by climate change. Improvements of our ocean and climate models are a necessary step to better understand the drivers of lower temperature and MHW trends in coastal regions, allowing for better predictive and management prospects of coastal marine ecosystems.

Acknowledgment

The authors acknowledge agencies and organisations responsible for providing data: the European Space Agency Climate Change Initiative and the Sea Surface Temperature Climate Change Initiative project together with the Centre for Environmental Data Analysis created and provided SST data available at https://catalogue.ceda.ac.uk/uuid/62c0f97b1eac4e0197a674870afe1ee6. The MGD data were obtained from the North-East Asian Regional Global Ocean Observing System (NEAR-GOOS) Regional Real Time Data Base (http://www.data.jma.go.jp/gmd/goos/data/pub/JMA-product/mgd_sst_glb_D/). OISST data were provided by the Physical Sciences Laboratory of National Oceanic and Atmospheric Administration/Earth System Research Laboratories, Boulder, Colorado (https://psl.noaa.gov/data/gridded/data.noaa.oisst.v2.highres.html). This research was undertaken with the assistance of resources from the National

Computational Infrastructure (NCI Australia), an NCRIS enabled capability supported by the Australian Government.

MM and MF are partly supported by a CAS-CSIRO collaboration project on comparative studies of marine ecosystems between Australia and China. MM acknowledges support from the Australian Research Centre for Climate Extremes. HP and NB acknowledge funding from the Earth Systems and Climate Change Hub of the Australian Government's National Environmental Science Program.

References

Bakun, A. (1990). Global climate change and intensification of coastal ocean upwelling. *Science*, *247*(4939), 198–201. https://doi.org/10.1126/science.247.4939.198Beggs, H. (2019). *Chapter 12: Temperature, In: Earth Observation: Data, Processing and Applications. Volume 3B: Applications – Surface Waters (Eds. Harrison, B.A., Anstee, J.A., Dekker, A., King, E., Phinn, S., Mueller, N., Byrne, G.) CRCSI, Melbourne*.Bonino, G., Masina, S., Iovino, D., Storto, A., & Tsujino, H. (2019). Eastern Boundary Upwelling Systems response to different atmospheric forcing in a global eddy-permitting ocean model. *Journal of Marine Systems*, *197*, 103178. https://doi.org/https://doi.org/10.1016/j.jmarsys.2019.05.004Chatterjee, A., Kumar, B. P., Prakash, S., & Singh, P. (2019). Annihilation of the Somali upwelling system during summer monsoon. *Scientific Reports*, *9*(1), 1–14. https://doi.org/10.1038/s41598-019-44099-1Dewitte, S., & Clerbaux, N. (2018). Decadal Changes of Earth's Outgoing Longwave Radiation. In *Remote Sensing* (Vol. 10, Issue 10). https://doi.org/10.3390/rs10101539Fiedler, E. K., McLaren, A., Banzon, V., Brasnett, B., Ishizaki, S., Kennedy, J., Rayner, N., Roberts-Jones, J., Corlett, G., Merchant, C. J., & Donlon, C. (2019). Intercomparison of long-term sea surface temperature analyses using the GHRSST Multi-Product Ensemble (GMPE) system. *Remote Sensing of Environment*, *222*(March 2018), 18–33. https://doi.org/10.1016/j.rse.2018.12.015Frölicher, T. L., Fischer, E. M., & Gruber, N. (2018). Marine heatwaves under global warming. *Nature*, *560*(7718), 360–364. https://doi.org/10.1038/s41586-018-0383-9García-Reyes, M., & Largier, J. (2010). Observations of increased wind-driven coastal upwelling off Central California. *Journal of Geophysical Research: Oceans*, *115*(4). https://doi.org/10.1029/2009JC005576Harris, R. M. B., Beaumont, L. J., Vance, T. R., Tozer, C. R., Remenyi, T. A., Perkins-Kirkpatrick, S. E., Mitchell, P. J., Nicotra, A. B., McGregor, S., Andrew, N. R., Letnic, M., Kearney, M. R., Wernberg, T., Hutley, L. B., Chambers, L. E., Fletcher, M.-S., Keatley, M. R., Woodward, C. A., Williamson, G., … Bowman, D. M. J. S. (2018). Biological responses to the press and pulse of climate trends and extreme events. *Nature Climate Change*, *8*(7), 579–587. https://doi.org/10.1038/s41558-018-0187-9Hayashida, H., Matear, R. J., Strutton, P. G., & Zhang, X. (2020). Insights into projected changes in marine heatwaves from a high-resolution ocean circulation model. *Nature Communi-*

cations, *11*(1), 1–9. https://doi.org/10.1038/s41467-020-18241-xHobday, A. J., Alexander, L. V, Perkins, S. E., Smale, D. A., Straub, S. C., Oliver, E. C. J., Benthuysen, J. A., Burrows, M. T., Donat, M. G., Feng, M., Holbrook, N. J., Moore, P. J., Scannell, H. A., Sen Gupta, A., & Wernberg, T. (2016). A hierarchical approach to defining marine heatwaves. *Progress in Oceanography*, *141*, 227–238. https://doi.org/http://dx.doi.org/10.1016/j.pocean.2015.12.014Kiss, A. E., Hogg, A. M., Hannah, N., Boeira Dias, F., Brassington, G. B., Chamberlain, M. A., Chapman, C., Dobrohotoff, P., Domingues, C. M., Duran, E. R., England, M. H., Fiedler, R., Griffies, S. M., Heerdegen, A., Heil, P., Holmes, R. M., Klocker, A., Marsland, S. J., Morrison, A. K., … Zhang, X. (2020). ACCESS-OM2 v1.0: a global ocean--sea ice model at three resolutions. *Geoscientific Model Development*, *13*(2), 401–442. https://doi.org/10.5194/gmd-13-401-2020Lee, T., Fukumori, I., & Tang, B. (2004). Temperature Advection: Internal versus External Processes. *Journal of Physical Oceanography*, *34*(8), 1936–1944. https://doi.org/10.1175/1520-0485(2004)034<1936:TAIVEP>2.0.CO;2Liang, S. (2017). Volume 5 overview: Recent progress in remote sensing of earth's energy budget. In *Comprehensive Remote Sensing* (Vols. 1–9). Elsevier. https://doi.org/10.1016/B978-0-12-409548-9.10365-3Lima, F. P., & Wethey, D. S. (2012). *Three decades of high-resolution coastal sea surface temperatures reveal more than warming*. *3*, 704. http://dx.doi.org/10.1038/ncomms1713Manizza, M., Le Quéré, C., Watson, A. J., & Buitenhuis, E. T. (2005). Bio-optical feedbacks among phytoplankton, upper ocean physics and sea-ice in a global model. *Geophysical Research Letters*, *32*(5). https://doi.org/https://doi.org/10.1029/2004GL020778Marin, M., Feng, M., Phillips, H. E., & Bindoff, N. L. (2021). A global, multi-product analysis of coastal marine heatwaves: distribution, characteristics and long-term trends. *Journal of Geophysical Research: Oceans*, *n/a*(n/a), e2020JC016708. https://doi.org/https://doi.org/10.1029/2020JC016708Marquis, J. W., Bogdanoff, A. S., Campbell, J. R., Cummings, J. A., Westphal, D. L., Smith, N. J., & Zhang, J. (2017). Estimating infrared radiometric satellite sea surface temperature retrieval cold biases in the tropics due to unscreened optically thin cirrus clouds. *Journal of Atmospheric and Oceanic Technology*, *34*(2), 355–373. https://doi.org/10.1175/JTECH-D-15-0226.1Merchant, C. J., Embury, O., Bulgin, C. E., Block, T., Corlett, G. K., Fiedler, E., Good, S. A., Mittaz, J., Rayner, N. A., Berry, D., Eastwood, S., Taylor, M., Tsushima, Y., Waterfall, A., Wilson, R., & Donlon, C. (2019). Satellite-based time-series of sea-surface temperature since 1981 for climate applications. *Scientific Data*, *6*(1), 223. https://doi.org/10.1038/s41597-019-0236-xNarayan, N., Paul, A., Mulitza, S., & Schulz, M. (2010). Trends in coastal upwelling intensity during the late 20th century. *Ocean Science*, *6*(3), 815–823. https://doi.org/10.5194/os-6-815-2010Oliver, E. C. J. (2019). Mean warming not variability drives marine heatwave trends. *Climate Dynamics*. https://doi.org/10.1007/s00382-019-04707-2Oliver, E. C. J., Benthuysen, J. A., Darmaraki, S., Donat, M. G., Hobday, A. J., Holbrook, N. J., Schlegel, R. W., & Sen Gupta, A. (2021). Marine Heatwaves. *Annual Review of Marine Science*, *13*(1), 313–342. https://doi.org/10.1146/annurev-marine-032720-095144Oliver, E. C. J., Donat,

M. G., Burrows, M. T., Moore, P. J., Smale, D. A., Alexander, L. V., Benthuysen, J. A., Feng, M., Sen Gupta, A., Hobday, A. J., Holbrook, N. J., Perkins-Kirkpatrick, S. E., Scannell, H. A., Straub, S. C., & Wernberg, T. (2018). Longer and more frequent marine heatwaves over the past century. *Nature Communications*, *9*(1). https://doi.org/10.1038/s41467-018-03732-9Patti, B., Guisande, C., Riveiro, I., Thejll, P., Cuttitta, A., Bonanno, A., Basilone, G., Buscaino, G., & Mazzola, S. (2010). Effect of atmospheric CO2 and solar activity on wind regime and water column stability in the major global upwelling areas. *Estuarine, Coastal and Shelf Science*, *88*(1), 45–52. https://doi.org/10.1016/j.ecss.2010.03.004Pilo, G. S., Holbrook, N. J., Kiss, A. E., & Hogg, A. M. C. (2019). Sensitivity of Marine Heatwave Metrics to Ocean Model Resolution. *Geophysical Research Letters*, *46*(24), 14604–14612. https://doi.org/10.1029/2019GL084928Qu, T., Du, Y., Strachan, J., Meyers, G., & Slingo, J. (2005). Sea surface temperature and its variability in the Indonesian region. *Oceanography*, *18*(SPL.ISS. 4), 50–61. https://doi.org/10.5670/oceanog.2005.05Rykaczewski, R. R., & Checkley, D. M. (2008). Influence of ocean winds on the pelagic ecosystem in upwelling regions. *Proceedings of the National Academy of Sciences of the United States of America*, *105*(6), 1965–1970. https://doi.org/10.1073/pnas.0711777105Seo, H., Brink, K. H., Dorman, C. E., Koracin, D., & Edwards, C. A. (2012). What determines the spatial pattern in summer upwelling trends on the U.S. West Coast? *Journal of Geophysical Research: Oceans*, *117*(8), 1–11. https://doi.org/10.1029/2012JC008016Simmons, H. L., Jayne, S. R., Laurent, L. C. S., & Weaver, A. J. (2004). Tidally driven mixing in a numerical model of the ocean general circulation. *Ocean Modelling*, *6*(3), 245–263. https://doi.org/https://doi.org/10.1016/S1463-5003(03)00011-8Small, R. J., Curchitser, E., Hedstrom, K., Kauffman, B., & Large, W. G. (2015). The Benguela Upwelling System: Quantifying the Sensitivity to Resolution and Coastal Wind Representation in a Global Climate Model. *Journal of Climate*, *28*(23), 9409–9432. https://doi.org/10.1175/JCLI-D-15-0192.1Stewart, K. D., Kim, W. M., Urakawa, S., Hogg, A. M., Yeager, S., Tsujino, H., Nakano, H., Kiss, A. E., & Danabasoglu, G. (2020). JRA55-do-based repeat year forcing datasets for driving ocean–sea-ice models. *Ocean Modelling*, *147*, 101557. https://doi.org/https://doi.org/10.1016/j.ocemod.2019.101557Sydeman, W. J., García-Reyes, M., Schoeman, D. S., Rykaczewski, R. R., Thompson, S. A., Black, B. A., & Bograd, S. J. (2014). Climate change and wind intensification in coastal upwelling ecosystems. *Science*, *345*(6192), 77–80. https://doi.org/10.1126/science.1251635Taboada, F. G., Stock, C. A., Griffies, S. M., Dunne, J., John, J. G., Small, R. J., & Tsujino, H. (2019). Surface winds from atmospheric reanalysis lead to contrasting oceanic forcing and coastal upwelling patterns. *Ocean Modelling*, *133*, 79–111. https://doi.org/https://doi.org/10.1016/j.ocemod.2018.11.003Tsujino, H., Urakawa, S., Nakano, H., Small, R. J., Kim, W. M., Yeager, S. G., Danabasoglu, G., Suzuki, T., Bamber, J. L., Bentsen, M., Böning, C. W., Bozec, A., Chassignet, E. P., Curchitser, E., Boeira Dias, F., Durack, P. J., Griffies, S. M., Harada, Y., Ilicak, M., … Yamazaki, D. (2018). JRA-55 based surface

dataset for driving ocean–sea-ice models (JRA55-do). *Ocean Modelling*, *130*, 79–139. https://doi.org/https://doi.org/10.1016/j.ocemod.2018.07.002Varela, R., Álvarez, I., Santos, F., DeCastro, M., & Gómez-Gesteira, M. (2015). Has upwelling strengthened along worldwide coasts over 1982-2010? *Scientific Reports*, *5*, 1–15. https://doi.org/10.1038/srep10016Varela, R., Rodríguez-Díaz, L., de Castro, M., & Gómez-Gesteira, M. (2021). Influence of Eastern Upwelling systems on marine heatwaves occurrence. *Global and Planetary Change*, *196*, 103379. https://doi.org/https://doi.org/10.1016/j.gloplacha.2020.103379Wu, J., Zha, J., Zhao, D., & Yang, Q. (2018). Changes in terrestrial near-surface wind speed and their possible causes: an overview. In *Climate Dynamics* (Vol. 51, Issues 5–6). Springer Berlin Heidelberg. https://doi.org/10.1007/s00382-017-3997-yZhang, Y., Feng, M., Du, Y., Phillips, H. E., Bindoff, N. L., & McPhaden, M. J. (2018). Strengthened Indonesian Throughflow Drives Decadal Warming in the Southern Indian Ocean. *Geophysical Research Letters*, *45*(12), 6167–6175. https://doi.org/https://doi.org/10.1029/2018GL078265Zhang, Z., Wang, K., Chen, D., Li, J., & Dickinson, R. (2019). Increase in surface friction dominates the observed surface wind speed decline during 1973-2014 in the northern hemisphere lands. *Journal of Climate*, *32*(21), 7421–7435. https://doi.org/10.1175/JCLI-D-18-0691.1Zhao, Z., & Marin, M. (2019). A MATLAB toolbox to detect and analyze marine heatwaves Software. In *Journal of Open Source Software* (Vol. 4). https://doi.org/10.21105/joss.01124